

CrossMark  
click for updates

Cite this: DOI: 10.1039/c5ta07040f

# Electronic structure, photovoltage, and photocatalytic hydrogen evolution with p-CuBi<sub>2</sub>O<sub>4</sub> nanocrystals†

Geetu Sharma,<sup>a</sup> Zeqiong Zhao,<sup>a</sup> Pranab Sarker,<sup>b</sup> Benjamin A. Nail,<sup>a</sup> Jiarui Wang,<sup>a</sup> Muhammad N. Huda\*<sup>b</sup> and Frank E. Osterloh\*<sup>a</sup>

As a visible light active p-type semiconductor, CuBi<sub>2</sub>O<sub>4</sub> is of interest as a photocatalyst for the generation of hydrogen fuel from water. Here we present the first photovoltage and photocatalytic measurements on this material and DFT results on its band structure. Single crystalline CuBi<sub>2</sub>O<sub>4</sub> nanoparticles (25.7 ± 4.7 nm) were synthesized from bismuth and cupric nitrate in water under hydrothermal conditions. Powder X-ray diffraction (XRD) confirms the CuBi<sub>2</sub>O<sub>4</sub> structure type and UV-Vis spectroscopy shows a 1.75 eV optical band gap. Surface photovoltage (SPV) measurements on CuBi<sub>2</sub>O<sub>4</sub> nanoparticle films on fluorine doped tin oxide yield 0.225 V positive photovoltage at >1.75 eV photon energy confirming holes as majority carriers. The photovoltage is reversible and limited by light absorption. When dispersed in 0.075 M aqueous potassium iodide solution, the CuBi<sub>2</sub>O<sub>4</sub> particles support photochemical hydrogen evolution of up to 16 μmol h<sup>-1</sup> under ultraviolet but not under visible light. Based on electrochemical scans, CuBi<sub>2</sub>O<sub>4</sub> is unstable toward reduction at -0.2 V, but a pH-dependent photocurrent of 6.45 μA cm<sup>-2</sup> with an onset potential of +0.75 V vs. NHE can be obtained with 0.01 M Na<sub>2</sub>S<sub>2</sub>O<sub>8</sub> as a sacrificial electron acceptor. The photoelectrochemical properties of CuBi<sub>2</sub>O<sub>4</sub> can be explained on the basis of the band structure of the material. DFT calculations show that the valence and conduction band edges arise primarily from the combination of O 2p and Cu 3d orbitals, respectively, with additional contributions from Cu 3d and Bi 6s orbitals just below the Fermi level. Trapping of photoelectrons in the Cu 3d band is the cause for reductive photocorrosion of the material, while the p-type conductivity arises from copper vacancy states near the VB edge. These findings provide an improved understanding of the photophysical properties of p-CuBi<sub>2</sub>O<sub>4</sub> and its limitations as a proton reduction photocatalyst.

Received 4th September 2015  
Accepted 26th December 2015

DOI: 10.1039/c5ta07040f

www.rsc.org/MaterialsA

## Introduction

Artificial photosynthesis of hydrogen from water is a promising avenue for the large scale production of carbon-free fuels.<sup>1</sup> The sunlight driven water splitting reaction is most efficiently accomplished with semiconductors linked in series using a Tandem or z-scheme configuration, like in natural photosynthesis.<sup>2-5</sup> Powdered photocatalysts for this process should be made of metal oxides to withstand the corrosive environment during water electrolysis.<sup>6</sup> While there are a great number of n-type metal oxides that function as photoanode materials, the regime of photocathodes is dominated by p-doped II-VI, III-V, and group IV compounds, including

p-CuGaSe<sub>2</sub>(CGS),<sup>7</sup> p-Cu<sub>2</sub>ZnSnS<sub>4</sub> (CZTS),<sup>8</sup> p-GaInP<sub>2</sub>,<sup>9</sup> p-GaN,<sup>10</sup> and p-Si.<sup>11</sup> Only a handful of visible light active p-metal oxides have been reported to date, many of which owe their p-type character to the presence of Cu(II) impurity states, as in Cu<sub>2</sub>O. Cuprous oxide itself is unstable under cathodic and anodic bias,<sup>12,13</sup> and the hope is to achieve greater stability in mixed metal oxides.<sup>14,15</sup> Many of these p-type oxides, incl. p-CuCrO<sub>2</sub>,<sup>16</sup> p-CuAlO<sub>2</sub>,<sup>17</sup> p-CuGaO<sub>2</sub>,<sup>18</sup> and p-CuFeO<sub>2</sub>,<sup>19,20</sup> crystallize in the ABX<sub>2</sub> delafossite structure type, where the linearly coordinated A cations form sheets and the B cations form edge-shared MO<sub>6</sub> octahedra. In 2007, Arai *et al.*, identified CuBi<sub>2</sub>O<sub>4</sub> during a combinatorial screening as a potential proton reduction photocathode.<sup>21,22</sup> Unlike delafossites, CuBi<sub>2</sub>O<sub>4</sub> contains stacks of square planar Cu(II)O<sub>4</sub> groups linked to distorted trigonal Bi(III)O<sub>6</sub> polyhedra.<sup>23</sup> Based on photocurrent measurements,<sup>22,24</sup> CuBi<sub>2</sub>O<sub>4</sub> is p-type and has an optical band gap of 1.8 eV.<sup>25</sup> In subsequent syntheses the material was obtained as films from electrochemical or chemical deposition followed by thermal annealing.<sup>24,25</sup> Pure CuBi<sub>2</sub>O<sub>4</sub> particles were obtained by solid state and hydrothermal syntheses.<sup>23,26-28</sup> The protocols by Xie<sup>26</sup> and Patil<sup>27</sup>

<sup>a</sup>Department of Chemistry, University of California, Davis. One Shields Avenue, Davis, CA, 95616, USA. E-mail: fosterloh@ucdavis.edu; Fax: +1 530 752 8995; Tel: +1 530 754 6242

<sup>b</sup>University of Texas Arlington, Department of Physics, Arlington, TX 76019, USA

† Electronic supplementary information (ESI) available: SPS schematics, profilometer, photoelectrochemical, and illumination data, DOS and defect diagrams. See DOI: 10.1039/c5ta07040f

afford nanoparticles of a dendritic shape, which is not optimal for integration into tandem photocatalysts, whereas the synthesis by Abdulkarem<sup>28</sup> can be tuned from dendritic nanostructures to nanorods, depending on the Cu precursor concentration. Here we report the first assessment of  $\text{CuBi}_2\text{O}_4$  nanocrystals as a suspended photocatalyst for  $\text{H}_2$  evolution, photovoltage data, and the results of DFT band structure calculations. The results show that while dry  $\text{CuBi}_2\text{O}_4$  nanocrystal films can generate over 200 mV reversible photovoltage under visible light illumination, the photoelectrochemical properties of wet films are limited by cathodic photocorrosion. According to DFT, photocorrosion is caused by trapping of photoelectrons in the Cu 3d band and the p-type conductivity of the material is due to copper vacancy states near the valence band edge.

## Results and discussion

$\text{CuBi}_2\text{O}_4$  was prepared by the published hydrothermal reaction,<sup>26</sup> after systematic optimization of reagent amounts. Transmission electron micrographs of the resulting  $\text{CuBi}_2\text{O}_4$  sample are shown in Fig. 1A. The particles are irregularly shaped with an average particle size of  $25.7 \pm 4.7$  nm. The crystallinity and phase confirmation of  $\text{CuBi}_2\text{O}_4$  by powder X-ray diffraction is presented in Fig. 1B. The XRD pattern matches the

JCPDS database (042-0334) and previous reports, respectively.<sup>24–28</sup> No peaks from impurity phases were observed.

The crystal size was estimated using the Scherrer equation from the diffraction peak widths at half maxima and was found to be about 28 nm. This means that the particles are single crystals.

Diffuse reflectance UV spectra were taken to obtain the Kubelka–Munk plot in Fig. 2A. Based on the absorption edge, the band gap of the material is 1.75 eV, close to the 1.80 eV value reported by Hahn *et al.*<sup>25</sup> This absorption is responsible for the brownish appearance of the material (inset in Fig. 2A). To investigate photochemical charge transfer in  $\text{CuBi}_2\text{O}_4$  nanoparticles, Surface Voltage Spectroscopy (SPS) was employed.<sup>29,30</sup> In this technique, a light-induced change of the contact potential difference (CPD, *versus* gold Kelvin probe) of a sample film is recorded as a function of the irradiation wavelength/energy (Fig. S1†).<sup>31</sup> Depending on the direction of charge transport, this produces either positive or negative photovoltage.

Spectra obtained in this way provide information about the carrier type,<sup>32</sup> mid gap states,<sup>33,34</sup> defects,<sup>35</sup> and electrochemical reactions at interfaces,<sup>36</sup> without the need for a liquid interface as in electrochemistry, for example. A spectrum of the  $\text{CuBi}_2\text{O}_4$  film on fluorine-doped tin oxide (FTO) is shown in Fig. 2A. The

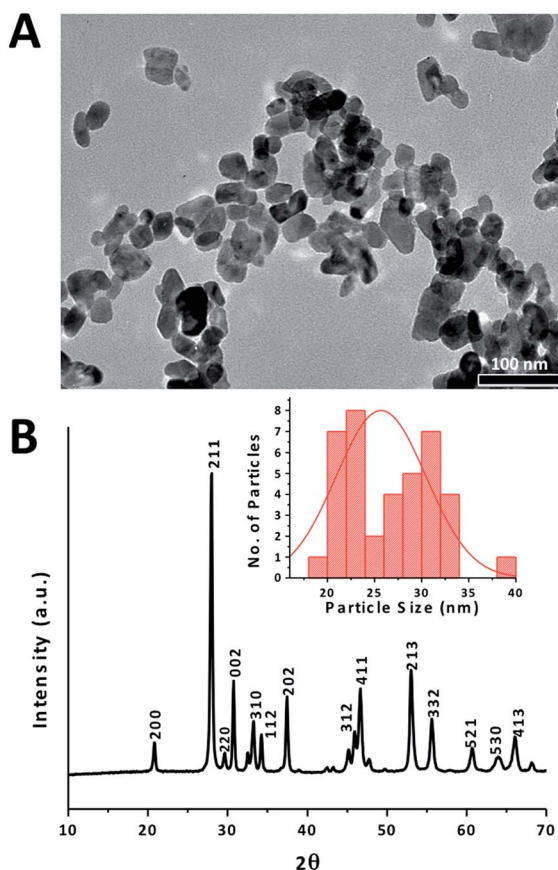


Fig. 1 (A) TEM images of  $\text{CuBi}_2\text{O}_4$  and size histogram. (B) Powder X-ray diffraction pattern with the index from JCPDS card 042-0334.

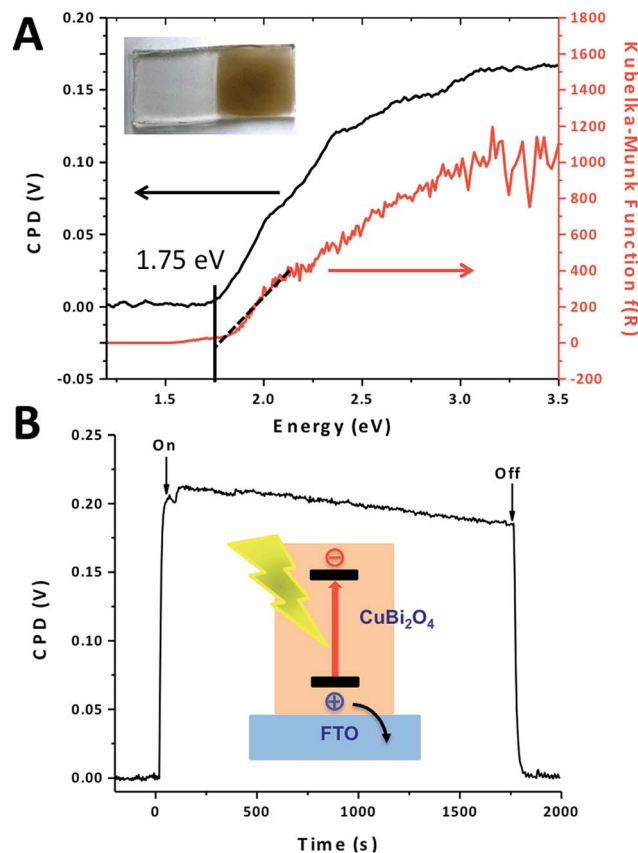


Fig. 2 (A) Kubelka Munk and surface photovoltage spectra of  $\text{CuBi}_2\text{O}_4$  on FTO substrates. (B) Time-dependent surface photovoltage spectrum of  $\text{CuBi}_2\text{O}_4$  nanoparticles under 2.71 eV monochromatic illumination ( $240 \mu\text{W cm}^{-2}$ ).

positive sign of  $\text{CuBi}_2\text{O}_4$  nanoparticles indicates the transport of holes towards the substrate and away from the Kelvin probe, as shown in the inset in Fig. 2B. This is similar to what was observed for  $\text{NiO}$ ,<sup>37</sup> and confirms the p-type character of  $\text{CuBi}_2\text{O}_4$ . The photoonset at 1.75 eV coincides with the optical band gap of  $\text{CuBi}_2\text{O}_4$ . This shows that the material is free from optically active defects. A time-dependent photovoltage measurement under 2.71 eV illumination (Fig. 2B) was performed to gain insight into the charge separation dynamics in a 4300 nm thick  $\text{CuBi}_2\text{O}_4$  film. On illumination, a stable positive signal (+0.21 V) develops within  $\sim 1$  s. When the light is turned off, the signal decays to zero over the same period of time. This fast and reversible charge separation indicates that deep charge traps are absent and that there is no significant photocorrosion under these conditions, as expected for a good photovoltaic material.<sup>38</sup>

Previous studies indicate a dependence of the maximum photovoltage on the absorber film thickness.<sup>32,39</sup> In order to study this effect, the  $\text{CuBi}_2\text{O}_4$  film thickness on FTO was varied. The spectra in Fig. 3 resemble those in Fig. 2, except for the

presence of local maxima at 2.0, 2.4, 2.7 and 3.1 eV. These are due to intensity variations of the Xe light source (spectrum in Fig. S1†).

For the thicker films, the maximum photovoltage shifts to 2.7 eV as a result of the lower light penetration depth at higher photon energy. The voltage increases monotonically with the film thickness, peaks at +0.239 V for the 7.2  $\mu\text{m}$  thick film, and then declines slightly to +0.227 V for the thickest film (10.3  $\mu\text{m}$ ). Assuming that 7.2  $\mu\text{m}$  thickness is required to absorb 99% of the photons, the optical penetration depth  $\delta_p$  at 2.7 eV can be estimated as 3.6  $\mu\text{m}$ , and the absorption coefficient  $\alpha = 2700 \text{ cm}^{-1}$ , according to  $\alpha = \delta_p^{-1}$ . Even though the 2.7 eV light no longer reaches the bottom 3  $\mu\text{m}$  of the 10.3  $\mu\text{m}$  film, the photovoltage only shows a minor decrease. This means that hole transport is very efficient in  $\text{CuBi}_2\text{O}_4$ , and the hole-diffusion length of the material is on the order of the film thickness (10  $\mu\text{m}$ ). This makes  $\text{CuBi}_2\text{O}_4$  interesting as a potential hole-conductor for solar cells,<sup>40–42</sup> and for thin film photovoltaics.<sup>43</sup> Based on the photovoltage data,  $\text{CuBi}_2\text{O}_4$  particles should also function as a proton photoreduction catalyst in the presence of a sacrificial donor. The  $\text{H}_2$  evolution performance of 50 mg of the material dispersed in 0.075 M KI solution is shown in Fig. 4. Indeed, after a small induction period,  $\text{CuBi}_2\text{O}_4$  produces  $\text{H}_2$  with rates of up to 16  $\mu\text{mol h}^{-1}$ , under UV/Vis illumination from a Xe arc lamp. However, the rate deteriorates after 6 h and the total amount of evolved  $\text{H}_2$  (95  $\mu\text{mol}$ ) only slightly exceeds the molar amount of the catalyst (91  $\mu\text{mol}$ ), corresponding to a TON of 1.1 over the 6 h illumination period. Under visible light illumination ( $>400 \text{ nm}$ ) no  $\text{H}_2$  is produced from KI solution, but small amounts ( $<1 \mu\text{mol}$ ) can be observed from aqueous methanol (Fig. S3†), even in the presence of platinum as a cocatalyst.

To determine the reasons for the low  $\text{H}_2$  evolution activity of  $\text{CuBi}_2\text{O}_4$ , photoelectrochemical scans of  $\text{CuBi}_2\text{O}_4$  films were

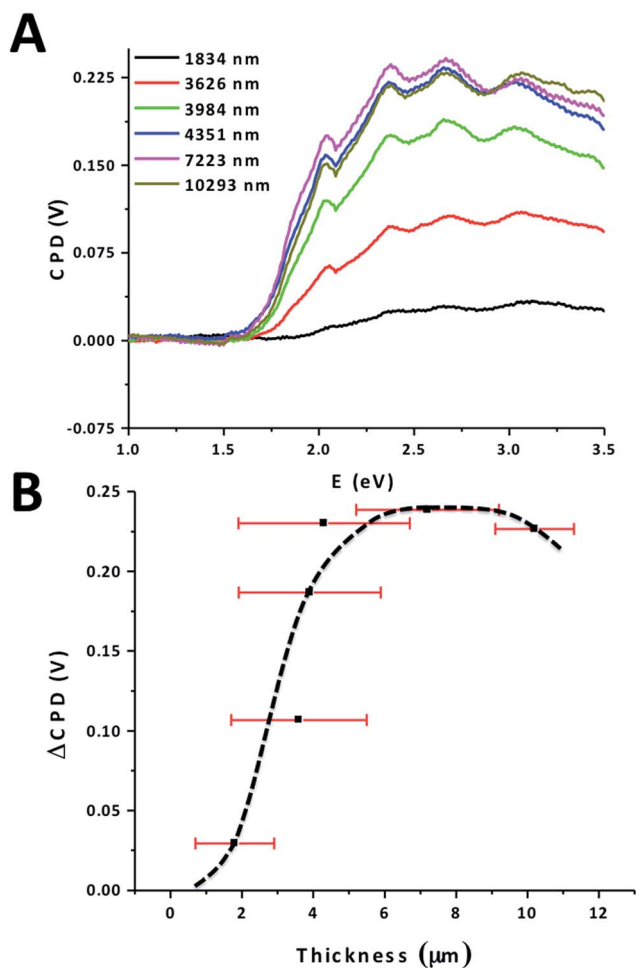


Fig. 3 (A) Surface photovoltage spectra of  $\text{CuBi}_2\text{O}_4$  nanoparticles on FTO and (B) peak photovoltage ( $\Delta\text{CPD}_{\text{max}}$ ) as a function of thickness (with error bars in red). Measurement configuration and Xe spectrum in Fig. S1.† Thickness determined by profilometry as shown in Fig. S2.† The hatched line is shown to emphasize the size trend.

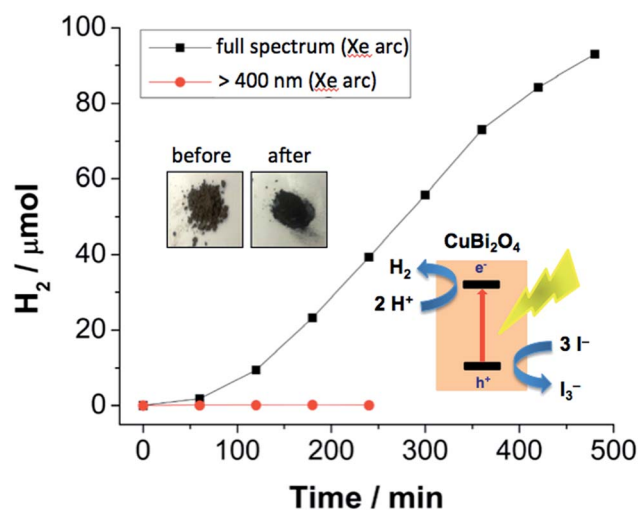


Fig. 4  $\text{H}_2$  evolution from 50 mg  $\text{CuBi}_2\text{O}_4$  nanoparticles in 100 mL of 0.075 M aqueous KI solution containing pH 7.2 buffer (0.05 M  $\text{NaH}_2\text{PO}_4$ /0.05 M  $\text{Na}_2\text{HPO}_4$ ) under visible ( $240 \text{ mW cm}^{-2}$  at the flask) or UV/Vis light ( $24 \text{ mW cm}^{-2}$  at the flask between 200 nm and 380 nm). Inset: photos of  $\text{CuBi}_2\text{O}_4$  powder before and after irradiation.

conducted under full spectrum illumination from a Xe lamp ( $40 \text{ mW cm}^{-2}$ ) as a function of pH. In aqueous  $0.1 \text{ M K}_2\text{SO}_4$  solution only very small cathodic photocurrents ( $<1 \mu\text{A cm}^{-2}$ ) were observed (Fig. S4<sup>†</sup>), but the addition of  $50 \text{ mg}$  of  $\text{Na}_2\text{S}_2\text{O}_8$  as a sacrificial electron acceptor boosts the current to above  $8 \mu\text{A cm}^{-2}$  (Fig. 5A). The size of the photocurrent is largest for basic solution and decreases monotonically as the pH is lowered to 3. At the same time, the photo-onset potentials shift from  $+0.87 \text{ V}$  vs. NHE for the pH 13 solution to  $+0.6 \text{ V}$  at pH 3. This shift is opposite of what would be expected from the Nernst equation,  $\delta E_F = -59 \text{ mV} \times \text{pH}$ ,<sup>23</sup> and has been previously attributed to the reduction of  $\text{CuBi}_2\text{O}_4$ .<sup>25</sup> Indeed, electrochemical scans in the dark (Fig. 5B) show the reduction of  $\text{CuBi}_2\text{O}_4$  at  $-0.2 \text{ V}$  vs. NHE (pH = 3), approximately  $0.5 \text{ V}$  before reduction of protons occurs (at  $-0.7 \text{ V}$  in pH = 3). At pH = 10 the reductive dark current is weaker, indicating improved stability of the material. This behaviour is similar to what was observed by the Buddie Mullins group.<sup>25</sup> Finally, under reductive bias,  $\text{CuBi}_2\text{O}_4$  films turn black (inset in Fig. 5B) similar to irradiated  $\text{CuBi}_2\text{O}_4$  particles in solution. This confirms that the photochemical deactivation under  $\text{H}_2$  evolution conditions is due to reduction.

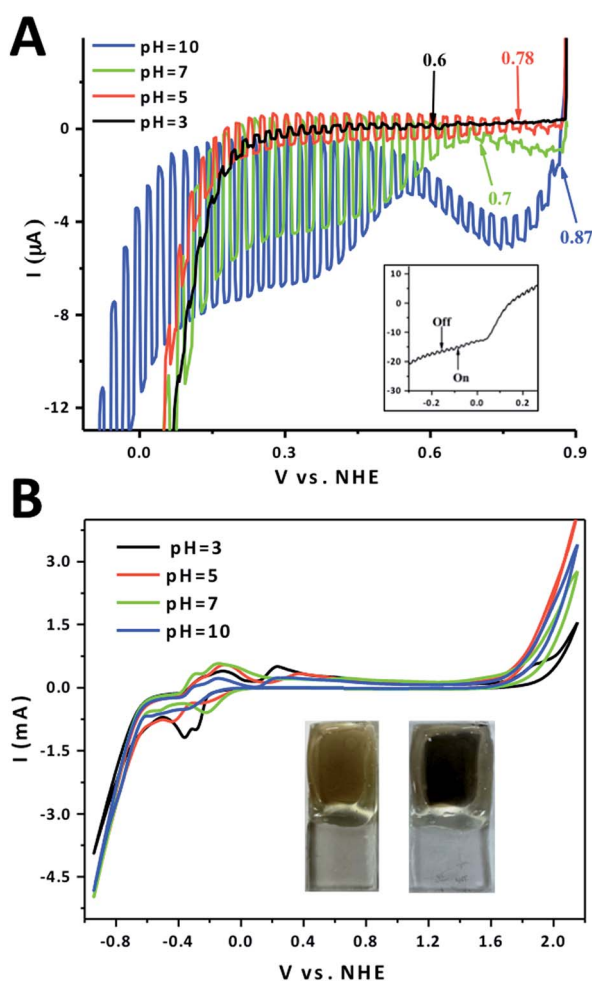


Fig. 5 Photocurrent (A) and dark (B) scans of  $\text{CuBi}_2\text{O}_4$  nanoparticles on FTO substrates in  $0.1 \text{ M K}_2\text{SO}_4$ ,  $50 \text{ mg Na}_2\text{S}_2\text{O}_8$  under different pH conditions. Light source: Xe arc lamp (full spectrum,  $40 \text{ mW cm}^{-2}$ ).

Finally, we employ DFT+U p-DOS (p: projected density of states; U: Hubbard-based correction parameter) calculations to analyze the photophysical properties of  $\text{CuBi}_2\text{O}_4$ . Fig. 6A shows the electronic band structures of  $\text{CuBi}_2\text{O}_4$  with and without copper vacancy defects. It can be seen that the direct band gap of pristine  $\text{CuBi}_2\text{O}_4$  of  $1.90 \text{ eV}$  at X is slightly higher than the experimentally observed one of  $1.75 \text{ eV}$ . This discrepancy can be overcome by introducing defects into the lattice. According to Fig. S5,<sup>†</sup> Cu vacancies and Cu substitution on Bi sites are the most probable defects under oxygen-rich single phase growth conditions (formation energies  $\sim 1.5 \text{ eV}$ ), but only the Cu vacancies reproduce the experimentally observed optical band gap of  $1.75 \text{ eV}$  (the band structure of  $\text{CuBi}_2\text{O}_4$  with Cu substitution defects is shown in Fig. S6<sup>†</sup>). These Cu vacancies also lead to empty states in the  $\text{CuBi}_2\text{O}_4$  valence band, explaining the observed p-type activity of the material. According to the p-DOS diagram in Fig. 6B, the valence and conduction band edges of  $\text{CuBi}_2\text{O}_4$  arise primarily from the combination of O 2p and Cu 3d orbitals, respectively, with additional contributions from the Cu 3d and Bi 6s orbitals just below the Fermi level. Trapping of photoelectrons in the Cu 3d band is the cause for the observed reductive photocorrosion of the material. Fig. 7 shows a simplified energy diagram of the compound together with electrochemical potentials of donors and acceptors. Visible

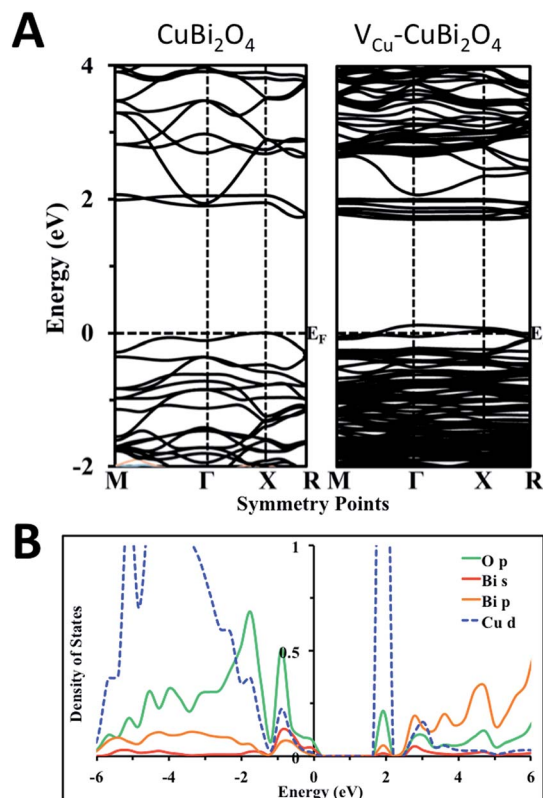


Fig. 6 (A) The DFT+U electronic band structures of (left) pristine  $\text{CuBi}_2\text{O}_4$  and (right)  $\text{V}_{\text{Cu}} - \text{CuBi}_2\text{O}_4$ . The Fermi level ( $E_F$ ) is set at  $0 \text{ eV}$ . The presence of  $\text{V}_{\text{Cu}}$  leads to partial occupation of the bands around the VB edge. This gives rise to p-type behavior in  $\text{CuBi}_2\text{O}_4$ . (B) The DFT+U projected density of states of  $\text{V}_{\text{Cu}} - \text{CuBi}_2\text{O}_4$ .

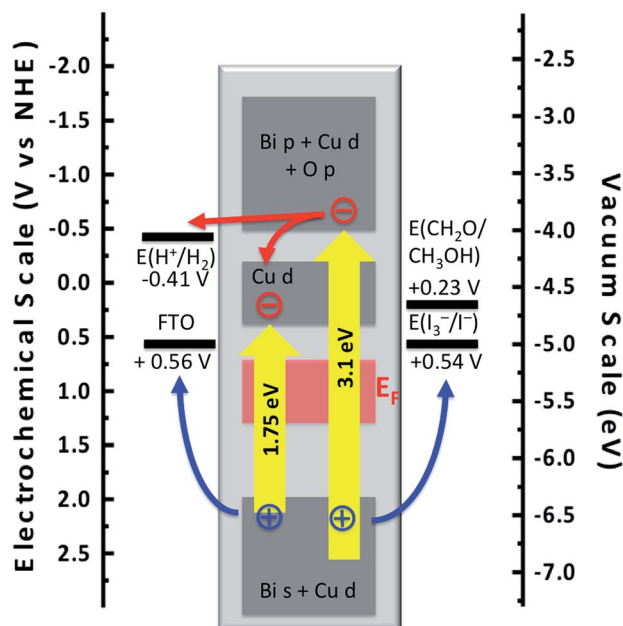


Fig. 7 Energy scheme of the  $\text{CuBi}_2\text{O}_4$  photocatalytic system at the point of zero charge.

light excitation (1.75–3.00 eV) of the material promotes electrons from the valence band into the Cu 3d band, while UV illumination (>3.1 eV) populates the more reducing Bi 3p states above. The Cu 3d band is positive of the proton reduction potential, but the Bi 3p band is not. This explains why hydrogen evolution from  $\text{CuBi}_2\text{O}_4$  requires UV excitation.

Fig. 7 also contains an estimate of the Fermi level of the material. Because of photocorrosion in solution, this value cannot be obtained from the cathodic photoonset potentials in Fig. 5A. Instead  $E_F$  is estimated from the photovoltage spectra in Fig. 3. Based on the +0.225 V experimental photovoltage, the Fermi level under illumination is located between +0.7 and +1.3 V, in the middle of the Cu d and O p valence band. Overall, Fig. 7 provides an understanding of the photochemical properties of the  $\text{CuBi}_2\text{O}_4/\text{H}_2\text{O}$  system and of the photovoltage of  $\text{CuBi}_2\text{O}_4$  films on FTO.

## Conclusions

In conclusion we have shown that well defined  $\text{CuBi}_2\text{O}_4$  nanocrystals can be obtained by hydrothermal synthesis of Cu and Bi nitrate in aqueous solution. Surface photovoltage measurements confirm the p-type character and a 1.75 eV effective band gap of the compound. Under vacuum,  $\text{CuBi}_2\text{O}_4$  nanocrystal films generate a reversible photovoltage of up to +225 mV with no apparent photocorrosion or trapping of charge carriers, but in  $\text{Na}_2\text{SO}_4$  electrolyte solution  $\text{CuBi}_2\text{O}_4$  undergoes reductive photocorrosion at  $-0.2$  V NHE. This electrochemical instability limits the ability of the compound to catalyse hydrogen evolution under visible light. DFT calculations show that the 1.75 eV band gap and the p-type conductivity of  $\text{CuBi}_2\text{O}_4$  are due to Cu vacancies in the lattice and that photocorrosion of the

compound is due to trapping of photoelectrons in the Cu d band near the conduction band edge. These findings provide an improved understanding of the photophysical properties of p- $\text{CuBi}_2\text{O}_4$ . Photocorrosion limits the use of  $\text{CuBi}_2\text{O}_4$  as a proton reduction photocatalyst, but the photovoltage data suggest that the material could find applications as an absorber for photovoltaic devices.

## Experimental

### Chemicals

$\text{Bi}(\text{NO}_3)_3 \cdot 5\text{H}_2\text{O}$  (Acros Organics, 99.9%),  $\text{CuSO}_4 \cdot 5\text{H}_2\text{O}$  (Merck, 98%), and NaOH (Fisher Scientific, 100%) were used as received. Water was purified to 18 M $\Omega$  cm resistivity using a Nano-pure system.

### Synthesis

Preparation of  $\text{CuBi}_2\text{O}_4$ .<sup>26</sup> In a typical experiment,  $\text{Bi}(\text{NO}_3)_3 \cdot 5\text{H}_2\text{O}$  (0.485 g, 1 mmol) was dissolved in 20 mL of water in the presence of conc. nitric acid (0.7 mL). After stirring for 2 h, a clear solution was obtained. Then, 10 mL aqueous  $\text{CuSO}_4 \cdot 5\text{H}_2\text{O}$  (0.124 g, 0.5 mmol) was added to the above solution which is followed by the addition of 15 mL of aqueous NaOH solution (1.0 M) until a green-blue precipitate is obtained. The complete mixture was then transferred into a Teflon lined autoclave, which was heated to 120 °C for 20 h. After cooling down to room temperature, the obtained black product was centrifuged, washed several times with water and dried under vacuum overnight to yield 0.256 g of product.

### Characterization

Powder XRD scans were performed using a Bruker D8 Advanced diffractometer with CuK radiation and a monochromatic wavelength of  $\lambda = 0.154$  nm. Transmission electron microscopy (TEM) images were recorded using a Philips CM12 at 120 kV. The samples for TEM were prepared by dispersing about 5 mg of sample in 2 mL of water by sonication for about 20 minutes. Then, about 20  $\mu\text{L}$  of suspended nanoparticles were dropped onto carbon coated Cu-grids using a micropipette and allowed to dry in air naturally. UV/Vis diffuse reflectance spectra were recorded on a Thermo Scientific Evolution 220 UV Vis spectrometer equipped with an integrating sphere. Surface photovoltage (SPV) measurements were conducted under vacuum ( $2.5 \times 10^{-4}$  mBar) on  $\text{CuBi}_2\text{O}_4$  films on FTO and gold substrates, respectively. A gold Kelvin probe (Delta PHI Besocke) served as the reference electrode. Samples were illuminated with monochromatic light from a 150 W Xe lamp filtered through an Oriel Cornerstone 130 monochromator ( $< 0.25$  mW  $\text{cm}^{-2}$ ). The CPD spectra were corrected for drift effects by subtracting a dark scan. For photoelectrochemical measurements, thin films of  $\text{CuBi}_2\text{O}_4$  nanoparticles were prepared by drop coating on F:SnO<sub>2</sub> (FTO) substrates followed by air annealing at 300 °C for 2 h. The  $\text{CuBi}_2\text{O}_4$  coated electrode was connected in a 3-electrode configuration with a Pt counter electrode and a saturated calomel reference electrode (SCE). Aqueous electrolyte solution (0.1 M  $\text{K}_2\text{SO}_4$ ) and an electron scavenger (50 mg,  $\text{Na}_2\text{S}_2\text{O}_8$ ) were

added to the cell and bubbled with  $N_2$  gas to remove all dissolved oxygen prior to scanning. The system was calibrated versus NHE using the redox potential of  $K_4[Fe(CN)_6]$  at +0.358 V vs. NHE. For photochemical  $H_2$  evolution, 50 mg of  $CuBi_2O_4$  was dispersed in 20% aqueous methanol or 0.075 M KI solutions containing 0.05 M  $NaH_2PO_4/0.05$  M  $Na_2HPO_4$  at pH 7.2 and the evolved gas was analyzed with a gas chromatograph (Varian 3800). All irradiation experiments were performed in a quartz flask using a 300 W Xe arc lamp with or without a sodium nitrite longpass (>400 nm) filter.

### Computations

DFT calculations were performed within the framework of the standard frozen-core projector augmented-wave (PAW)<sup>44,45</sup> method as implemented in the Vienna *ab initio* simulation package (VASP)<sup>46,47</sup> code. Exchange and correlation potentials were treated in the generalized gradient approximation (GGA) as parameterized by Perdew–Burke–Ernzerhof (PBE).<sup>48,49</sup> The basis sets were expanded with plane waves with a kinetic-energy cut-off of 400 eV. The shortcomings of DFT—*i.e.*, the underestimation of electron localization for systems with localized d and f electrons<sup>50–52</sup> were rectified using the Hubbard U parameter.<sup>50,53,54</sup> In the present work, we have used  $U_{\text{eff}} = 6$  eV, ( $U_{\text{eff}} = U - J = 7 - 1 = 6$  eV,  $J =$  Stoner exchange parameter), which externally provides a Coulomb correlation with the Cu 3d orbital. We chose this value of  $U_{\text{eff}}$  to be consistent with the previous work on a Cu–Bi–O derived compound.<sup>55</sup> A  $9 \times 9 \times 13$  Monkhorst–Pack<sup>56</sup>  $k$ -point sampling was used for ion relaxation; however, density-of-states (DOS) and optical absorption calculations were done with higher  $11 \times 11 \times 13$   $k$ -point sampling. For the defect calculations, we constructed a supercell containing 112 atoms. A  $5 \times 3 \times 5$   $k$ -point sampling was used for defect-induced calculations.

### Acknowledgements

FEO acknowledges Research Corporation for Science Advancement for a Scialog award and the National Science Foundation for financial support through grants 1152250 and 1133099. All computations were performed using the High Performance Computing Facility (HPCF) at the University of Texas at Arlington and at the Texas Advanced Computing Center (TACC).

### Notes and references

- 1 F. E. Osterloh, *Chem. Mater.*, 2008, **20**, 35–54.
- 2 M. G. Walter, E. L. Warren, J. R. McKone, S. W. Boettcher, Q. X. Mi, E. A. Santori and N. S. Lewis, *Chem. Rev.*, 2010, **110**, 6446–6473.
- 3 A. Kudo, *MRS Bull.*, 2011, **36**, 32–38.
- 4 K. Maeda, *ACS Catal.*, 2013, **3**, 1486–1503.
- 5 T. Hisatomi, J. Kubota and K. Domen, *Chem. Soc. Rev.*, 2014, **43**, 7520–7535.
- 6 D. M. Fabian, S. Hu, N. Singh, F. A. Houle, T. Hisatomi, K. Domen, F. E. Osterloh and S. Ardo, *Energy Environ. Sci.*, 2015, **8**, 2825–2850.
- 7 M. Moriya, T. Minegishi, H. Kumagai, M. Katayama, J. Kubota and K. Domen, *J. Am. Chem. Soc.*, 2013, **135**, 3733–3735.
- 8 L. Rovelli, S. D. Tilley and K. Sivula, *ACS Appl. Mater. Interfaces*, 2013, **5**, 8018–8024.
- 9 O. Khaselev and J. A. Turner, *Science*, 1998, **280**, 425–427.
- 10 M. G. Kibria, S. Zhao, F. A. Chowdhury, Q. Wang, H. P. T. Nguyen, M. L. Trudeau, H. Guo and Z. Mi, *Nat. Commun.*, 2014, **5**, 3825, DOI: 10.1038/ncomms4825.
- 11 S. W. Boettcher, E. L. Warren, M. C. Putnam, E. A. Santori, D. Turner-Evans, M. D. Kelzenberg, M. G. Walter, J. R. McKone, B. S. Brunschwig, H. A. Atwater and N. S. Lewis, *J. Am. Chem. Soc.*, 2011, **133**, 1216–1219.
- 12 A. Paracchino, V. Laporte, K. Sivula, M. Graetzel and E. Thimsen, *Nat. Mater.*, 2011, **10**, 456–461.
- 13 S. Kakuta and T. Abe, *Electrochem. Solid-State Lett.*, 2009, **12**, P1–P3.
- 14 U. A. Joshi and P. A. Maggard, *J. Phys. Chem. Lett.*, 2012, **3**, 1577–1581.
- 15 U. A. Joshi, A. M. Palasyuk and P. A. Maggard, *J. Phys. Chem. C*, 2011, **115**, 13534–13539.
- 16 S. Powar, D. Xiong, T. Daeneke, M. T. Ma, A. Gupta, G. Lee, S. Makuta, Y. Tachibana, W. Chen, L. Spiccia, Y.-B. Cheng, G. Götz, P. Bäuerle and U. Bach, *J. Phys. Chem. C*, 2014, **118**, 16375–16379.
- 17 H. Kawazoe, M. Yasukawa, H. Hyodo, M. Kurita, H. Yanagi and H. Hosono, *Nature*, 1997, **389**, 939–942.
- 18 A. Renaud, B. Chavillon, L. le Pleux, Y. Pellegrin, E. Blart, M. Boujtita, T. Pauporte, L. Cario, S. Jobic and F. Odobel, *J. Mater. Chem.*, 2012, **22**, 14353–14356.
- 19 C. G. Read, Y. Park and K.-S. Choi, *J. Phys. Chem. Lett.*, 2012, **3**, 1872–1876.
- 20 M. S. Prévot, N. Guijarro and K. Sivula, *ChemSusChem*, 2015, **8**, 1359–1367.
- 21 T. Arai, M. Yanagida, Y. Konishi, Y. Iwasaki, H. Sugihara and K. Sayama, *J. Phys. Chem. C*, 2007, **111**, 7574–7577.
- 22 T. Arai, Y. Konishi, Y. Iwasaki, H. Sugihara and K. Sayama, *J. Comb. Chem.*, 2007, **9**, 574–581.
- 23 R. Arpe and H. Müller-Buschbaum, *Z. Anorg. Allg. Chem.*, 1976, **426**, 1–6.
- 24 H. S. Park, C.-Y. Lee and E. Reisner, *Phys. Chem. Chem. Phys.*, 2014, **16**, 22462–22465.
- 25 N. T. Hahn, V. C. Holmberg, B. A. Korgel and C. B. Mullins, *J. Phys. Chem. C*, 2012, **116**, 6459–6466.
- 26 Y. Xie, Y. Zhang, G. Yang, C. Liu and J. Wang, *Mater. Lett.*, 2013, **107**, 291–294.
- 27 R. Patil, S. Kelkar, R. Naphade and S. Ogale, *J. Mater. Chem. A*, 2014, **2**, 3661–3668.
- 28 A. M. Abdulkarem, J. Li, A. A. Aref, L. Ren, E. M. Elssfah, H. Wang, Y. Ge and Y. Yu, *Mater. Res. Bull.*, 2011, **46**, 1443–1450.
- 29 L. Kronik and Y. Shapira, *Surf. Sci. Rep.*, 1999, **37**, 1–206.
- 30 T. Dittrich, S. Bonisch, P. Zabel and S. Dube, *Rev. Sci. Instrum.*, 2008, **79**, 113903.
- 31 J. Zhao and F. E. Osterloh, *J. Phys. Chem. Lett.*, 2014, **5**, 782–786.

- 32 Y. Yang, J. Wang, J. Zhao, B. A. Nail, X. Yuan, Y. Guo and F. E. Osterloh, *ACS Appl. Mater. Interfaces*, 2015, **10**, 5959–5964.
- 33 F. E. Osterloh, M. A. Holmes, J. Zhao, L. Chang, S. Kawula, J. D. Roehling and A. J. Moulé, *J. Phys. Chem. C*, 2014, **118**, 14723–14731.
- 34 F. E. Osterloh, M. A. Holmes, L. Chang, A. J. Moule and J. Zhao, *J. Phys. Chem. C*, 2013, **117**, 26905–26913.
- 35 P. Wu, J. Wang, J. Zhao, L. Guo and F. E. Osterloh, *J. Mater. Chem. A*, 2014, **2**, 20338–20344.
- 36 J. Wang, J. Zhao and F. E. Osterloh, *Energy Environ. Sci.*, 2015, **8**, 2970–2976.
- 37 B. A. Nail, J. M. Fields, J. Zhao, J. Wang, M. J. Greaney, R. L. Brutchey and F. E. Osterloh, *ACS Nano*, 2015, **9**, 5135–5142.
- 38 S. Merdes, F. Osterloh, R. Sáez-Araoz, J. Klaer, R. Klenk and T. Dittrich, *Appl. Phys. Lett.*, 2013, **102**, 213902.
- 39 E. Zillner and T. Dittrich, *Phys. Status Solidi RRL*, 2011, **5**, 256–258.
- 40 G. Natu, P. Hasin, Z. J. Huang, Z. Q. Ji, M. F. He and Y. Y. Wu, *ACS Appl. Mater. Interfaces*, 2012, **4**, 5922–5929.
- 41 A. Nattestad, A. J. Mozer, M. K. R. Fischer, Y. B. Cheng, A. Mishra, P. Bauerle and U. Bach, *Nat. Mater.*, 2010, **9**, 31–35.
- 42 F. Odobel and Y. Pellegrin, *J. Phys. Chem. Lett.*, 2013, **4**, 2551–2564.
- 43 S. E. Habas, H. A. S. Platt, M. van Hest and D. S. Ginley, *Chem. Rev.*, 2010, **110**, 6571–6594.
- 44 G. Kresse and D. Joubert, *Phys. Rev. B: Condens. Matter Mater. Phys.*, 1999, **59**, 1758–1775.
- 45 P. E. Blochl, *Phys. Rev. B: Condens. Matter Mater. Phys.*, 1994, **50**, 17953–17979.
- 46 G. Kresse and J. Furthmuller, *Phys. Rev. B: Condens. Matter Mater. Phys.*, 1996, **54**, 11169–11186.
- 47 G. Kresse and J. Furthmuller, *Comput. Mater. Sci.*, 1996, **6**, 15–50.
- 48 J. P. Perdew, J. A. Chevary, S. H. Vosko, K. A. Jackson, M. R. Pederson, D. J. Singh and C. Fiolhais, *Phys. Rev. B: Condens. Matter Mater. Phys.*, 1992, **46**, 6671–6687.
- 49 J. P. Perdew, K. Burke and M. Ernzerhof, *Phys. Rev. Lett.*, 1996, **77**, 3865–3868.
- 50 V. I. Anisimov, J. Zaanen and O. K. Andersen, *Phys. Rev. B: Condens. Matter Mater. Phys.*, 1991, **44**, 943–954.
- 51 F. Zhou, C. A. Marianetti, M. Cococcioni, D. Morgan and G. Ceder, *Phys. Rev. B: Condens. Matter Mater. Phys.*, 2004, **69**, 201101.
- 52 M. V. Ganduglia-Pirovano, A. Hofmann and J. Sauer, *Surf. Sci. Rep.*, 2007, **62**, 219–270.
- 53 V. I. Anisimov, I. V. Solovyev, M. A. Korotin, M. T. Czyzyk and G. A. Sawatzky, *Phys. Rev. B: Condens. Matter Mater. Phys.*, 1993, **48**, 16929–16934.
- 54 I. V. Solovyev, P. H. Dederichs and V. I. Anisimov, *Phys. Rev. B: Condens. Matter Mater. Phys.*, 1994, **50**, 16861–16871.
- 55 P. Sarker, D. Prasher, N. Gaillard and M. N. Huda, *J. Appl. Phys.*, 2013, **114**, 133508.
- 56 H. J. Monkhorst and J. D. Pack, *Phys. Rev. B: Condens. Matter Mater. Phys.*, 1976, **13**, 5188–5192.